Extreme Mechanics Letters 3 (2015) 130–140

Contents lists available at ScienceDirect

Extreme Mechanics Letters

journal homepage: www.elsevier.com/locate/eml

Wet adhesion of graphene

Wei Gao, Kenneth M. Liechti, Rui Huang*

Department of Aerospace Engineering and Engineering Mechanics, University of Texas, Austin, TX 78712, United States

ARTICLE INFO

Article history:
Received 8 March 2015
Received in revised form 8 April 2015
Accepted 8 April 2015
Available online 12 April 2015

Keywords:
Adhesion
Graphene
Water
Cavitation
Capillary bridging

ABSTRACT

Interfacial adhesion between graphene and various substrate materials is essential for practical applications of graphene. To date, most of the studies on adhesion of graphene have assumed dry adhesion of van der Waals type. In this paper, we conduct molecular dynamics simulations to study the traction–separation behaviors for wet adhesion of graphene on amorphous silicon oxide covered by a thin layer of water. Three stages of the traction–separation relations are identified and they are analyzed by simple, approximate continuum models. The work of separation is found to be close to the theoretical value dictated by the interaction potential between graphene and water. The maximum traction is found to be set by the critical stress for cavitation at the water/graphene interface. With morphological evolution of water from cavitation to capillary bridging, the range of interaction extends to about 3 nm before complete separation of graphene. Compared to van der Waals interactions for dry adhesion of graphene, the work of separation for wet adhesion is smaller, the maximum traction is lower, but the interaction range is longer. It is noted that the properties of wet adhesion depend sensitively on the graphene–water interactions, which may vary considerably from hydrophobic to hydrophilic interactions.

1. Introduction

As an extremely thin crystal membrane, graphene has been studied extensively over the last decade for its physical properties and potential applications. In particular, the interfacial adhesion between graphene and various substrate materials is essential for the manufacture and integration of graphene [1–4]. To date, most of the studies on adhesion of graphene have assumed dry adhesion of van der Waals type [5–9]. However, measurements of the adhesion energy of graphene are often performed in ambient conditions [10–15], not in high vacuum. The results are likely influenced by the presence of water at the interfaces, depending on relative humidity of the environment. In the case of wet-transferred graphene [1,15], both the graphene membrane and its substrate are directly exposed to liquid water during fabrication. A recent experimental study reported ultra-long-range interactions between wet-transferred graphene and a silicon substrate [15], calling for further studies on other mechanisms of interfacial adhesion of graphene. This paper presents the first study on wet adhesion of graphene. We consider a relatively simple system with a pristine graphene monolayer on an amorphous silicon oxide (a-SiO_2) substrate, where a thin layer of water is sandwiched in between (see Fig. 1).

Previous studies [16–18] have shown that the silanol groups on SiO_2 surfaces are sensitive to the adsorption of water molecules (H_2O). Lee et al. [19] showed that water could diffuse between monolayer graphene and SiO_2 substrates under high humidity conditions. The water diffusion results in the formation of a double ice-like water layer, which is quite stable, even under ambient conditions. Additional highly mobile and volatile liquid phase water can further diffuse between graphene and the ice-like layer on the SiO_2 substrate. On the other hand, graphene is generally considered to be hydrophobic, with

* Corresponding author.
E-mail address: ruihuang@mail.utexas.edu (R. Huang).

http://dx.doi.org/10.1016/j.eml.2015.04.003
2352-4316/

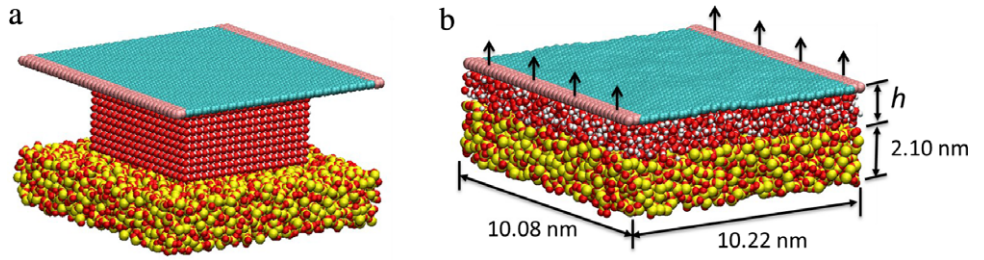

Fig. 1. (a) Initial model with a box of water molecules; (b) Relaxed model with a continuous water film between a graphene monolayer and an a-SiO_2 substrate. The atoms are colored as Si (yellow), O (red), H (white), and C (green and pink). The pink C atoms are fixed during relaxation. During separation, the pink C atoms are pulled upwards with increasing displacement, while the atoms in the lower half of the a-SiO_2 substrate are fixed. (For interpretation of the references to color in this figure legend, the reader is referred to the web version of this article.)

a contact angle of ∼90° [20–24], although some recent studies have found that the contact angle of water on graphene could vary over a wide range, depending on airborne contamination [25,26], defects [21], roughness [27], and the substrate on which it has been deposited [28,29]. In principle, the contact angle can be related to the interactions between graphene and water. In this paper we adopt a model assuming hydrophobic interactions with a contact angle of ∼90° for graphene. Molecular dynamics (MD) simulations are conducted to investigate the separation process with a sequence of morphological transitions of water between graphene and a-SiO_2 substrate. Approximate continuum analyses are developed to help understand the MD results. Section 2 presents the model and method for MD simulations. The results are discussed in Section 3, followed by a summary in Section 4.

2. MD model and method

All MD simulations in this study are performed with LAMMPS [30] in NVT ensemble at 300 K using the Nose–Hoover thermostat with an integration time step of 1 fs. As shown in Fig. 1, the MD model includes a monolayer graphene sheet and an a-SiO_2 substrate. Initially, a box of water molecules is placed between a-SiO_2 and graphene (Fig. 1(a)). The system is then relaxed at 300 K, while two edges of the graphene (colored in pink) are fixed. During relaxation, the water molecules spread out on the surface of a-SiO_2 and the substrate is pulled up towards graphene. After a sufficiently long time, the system reaches an equilibrium state, with a continuous water film between graphene and a-SiO_2, as shown in Fig. 1(b). Periodic boundary conditions are applied in all three directions. The in-plane dimensions of the periodic box are set by the graphene sheet in its ground state (about 10 nm by 10 nm), while the a-SiO_2 substrate is subjected to a small biaxial strain (∼0.3%) to accommodate the mismatch with graphene. The a-SiO_2 substrate is about 2 nm thick, and the thickness of the water film is varied from 1 to 4 nm by changing the number of water molecules; this thickness range is chosen to illustrate three different behaviors. The height of the periodic box is much larger (40 nm) to prevent interactions between periodic images in the thickness direction.

Simulations of the separation processes are conducted by increasing the prescribed displacement in the normal direction for the carbon (C) atoms along the two clamped edges of the graphene, while the atoms in the lower half of the a-SiO_2 substrate are fixed. The displacement is applied stepwise, with an increase of 0.1 Å at each step followed by relaxation for 1 ns (10^6 time steps). At each separation displacement, we compute the total interaction force between graphene and the substrate (including water), with which the average traction is obtained as a function of the displacement:

$$\sigma(d) = \frac{\langle F(d)\rangle_t}{A}, \tag{1}$$

where A is the area of the undeformed graphene sheet, d is the prescribed edge displacement, and $\langle F(d)\rangle_t$ denotes the time average of the total force as a function of d. Using this molecular model, we study the traction–separation relation for wet adhesion of graphene and associated mechanisms.

The MD simulations employ a set of empirical force fields. The second-generation reactive empirical bond-order potential (REBO) is used to describe the C–C interactions in graphene [31]. Previous studies [32–36] have shown that the REBO potential provides reasonable predictions of the mechanical properties of monolayer graphene. For the a-SiO_2 substrate, we use the Tersoff potential [37], with a parameter set developed by Munetoh et al. [38] for the Si–O systems. The Tersoff potential is computationally efficient and predicts accurate mechanical properties of SiO_2 in comparison with *ab initio* calculations and experimental data [38]. The water molecules are described by the extended simple point charge (SPC/E) model [39], characterized by three point masses with the O–H bond distance of 0.1 nm and H–O–H bond angle equal to 109.47°. The constraints on the bond length and bond angle within each water molecule are enforced through the SHAKE algorithm [40]. The interatomic potential energy for water is given by:

$$U_{ij}^{\text{water}} = 4\varepsilon_{ij}\left[\left(\frac{\delta_{ij}}{r_{ij}}\right)^{12} - \left(\frac{\delta_{ij}}{r_{ij}}\right)^{6}\right] + \frac{k_e q_i q_j}{r_{ij}}, \tag{2}$$

where i and j are indices for either O or H atoms of water, r_{ij} is the interatomic distance, and k_e is the electrostatic constant (8.987×10^9 N m^2/C^2). The potential energy includes two parts: the dispersion interactions represented by the Lennard-Jones (LJ) potential with two parameters (δ_{ij} and

ε_{ij}) for each pair and the electrostatic interactions between charges q_i and q_j. According to the SPC/E model [39], the charges on O and H are −0.8476 and 0.4238 e, respectively. Meanwhile, only the O–O interactions are included for the LJ potential with parameters $\delta_{OO} = 0.3166$ nm and $\varepsilon_{OO} = 6.76$ meV; the O–H and H–H dispersion interactions are much weaker and hence ignored. In MD simulations, the cutoff distances for the interactions are set to be 1 nm for the dispersion interactions and 1.2 nm for the electrostatic interactions, following common practice [39]; the longer cut-off distance for the electrostatic interactions may be justified by noting the slower decay with increasing interatomic distance. The long-range electrostatic interactions are computed by using the particle–particle particle–mesh (PPPM) algorithm [41] as implemented in LAMMPS.

The mechanical property of water is essential for the present study. It is often assumed in theoretical analyses that water in its liquid phase is incompressible. However, measurements have found that the bulk modulus of liquid water is about 2.2 GPa [42]. Using the SPC/E model for water, we perform MD simulations of water under hydrostatic tension at 300 K. In our calculation, a box of water molecules with periodic boundary conditions is subjected to an increasing volumetric strain (stepwise loading with displacement in all three directions, followed by relaxation at each step), and the virial stress is calculated as a function of the volumetric strain. As shown in Fig. 2, the average stress (hydrostatic tension) in water first increases with the volumetric strain, giving an initial bulk modulus of 2.07 GPa, close to the measured value. Moreover, the hydrostatic tension increases nonlinearly and reaches a maximum of 142.2 MPa, beyond which the stress drops with increasing strain. The maximum hydrostatic tension is associated with onset of cavitation in water and weakly depends on the size of the computational box. The critical stress for cavitation in water has been previously reported as ranging from 100 to 200 MPa at room temperature [43–45]. Therefore, the SPC/E model captures the mechanical behavior of water reasonably well.

In addition to the force fields for graphene, a-SiO_2 and water, interfacial force fields are needed to describe the interactions among them. First-principle calculations [9,46] have shown that the interactions between graphene and water is dominated by dispersion interactions. Based on the contact angle and the water monomer binding energy on graphite, Werder et al. [47] calibrated a set of parameters for the LJ potential interacting between the oxygen atoms of water and the carbon atoms; the interactions between the hydrogen atoms of water and the carbon atoms were ignored. The LJ potential function takes the same form as the first term on the right-hand side of Eq. (2), with fitted parameters $\delta_{CO} = 0.319$ nm and $\varepsilon_{CO} = 4.07$ meV. These parameters lead to a theoretical adhesion energy of 60.0 mJ/m^2 between water and graphene, with an equilibrium separation of 0.274 nm [48]. Using this interaction potential along with the SPC/E model for water, we performed an MD simulation to determine the contact angle of a water droplet on graphene. As shown in Fig. 3, a box of water molecules relax to form a hemispherical droplet on graphene, with a contact angle of about 90°. Different contact angles may be obtained by modifying the fitted parameters (δ_{CO} and ε_{CO}), which is left for future studies.

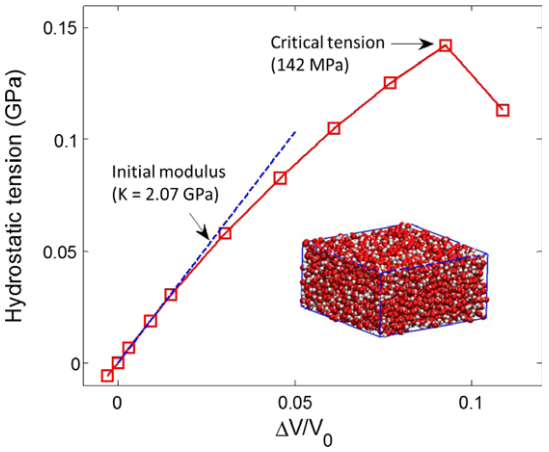

Fig. 2. Nonlinear hydrostatic stress–strain relation of bulk water obtained from MD simulations using the SPC/E model. Inset shows the box of water molecules subjected to hydrostatic tension. The dashed line shows the linear approximation with an initial bulk modulus of 2.07 GPa for small strains. The maximum tension is associated with the onset of cavitation in water.

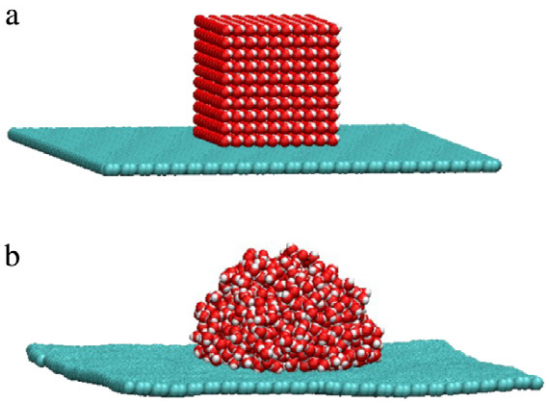

Fig. 3. (a) A box of water molecules on graphene before relaxation, and (b) a hemispherical water droplet after relaxation at 300 K, with a contact angle of about 90°.

The force field developed by Cruz-Chu et al. [49] is adopted for water–SiO_2 interaction, which includes both electrostatic and van der Waals forces. Similar to the potential function in Eq. (2), the LJ parameters for the Si–O and O–O interactions are: $\delta_{SiO} = 0.347$ nm, $\varepsilon_{SiO} = 2.30$ meV, $\delta_{OO} = 0.382$ nm, and $\varepsilon_{OO} = 1.63$ meV, while the H atoms are ignored. The charges for the Si and O atoms in SiO_2 are set to be 1 and −0.5 e, respectively. These parameters are chosen so that the surface of a-SiO_2 is superhydrophilic with a contact angle of almost 0°. However, as observed in previous studies [49,50], the water–SiO_2 interactions could be much more complicated, requiring empirical parameters to account for other surface characteristics of SiO_2, which are beyond the scope of the present study.

Finally, the interaction between graphene and a-SiO_2 (without water) is assumed to be primarily due to van der Waals forces. According to the previous studies [9,51,52], the range of the van der Waals forces between graphene

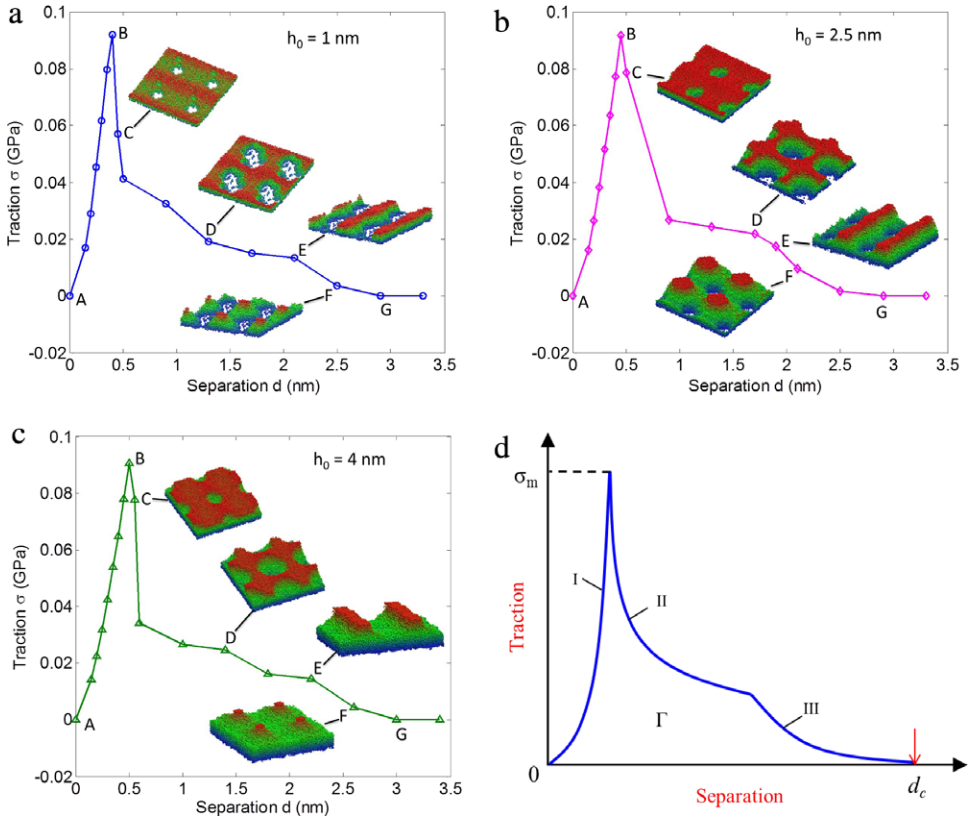

Fig. 4. (a)–(c) Traction–separation relations for graphene on a-SiO_2 with a water film of initial thickness equal to 1, 2.5, and 4 nm, respectively. The insets are snapshots (2 by 2 periodic replication) from the MD simulations showing only the water molecules, with colors for the height contours. (d) A schematic illustration of the three stages in the traction–separation relation: (I) continuous water film (A–B), (II) cavitation (C–D), and (III) capillary bridging (E–F). Note the maximum traction σ_m, range of interaction d_c and the work of separation Γ. (For interpretation of the references to color in this figure legend, the reader is referred to the web version of this article.)

and a-SiO_2 is about 1 nm, beyond which the interaction is negligible. For computational efficiency and based on the fact that the thickness of the water layer considered in this study is equal to or greater than 1 nm, the van der Waals forces between graphene and a-SiO_2 were not included in the MD simulations.

The a-SiO_2 substrate in the MD simulations is obtained by a melt–quench–relaxation procedure, following the recipe of Litton and Garofalini [53]. We start by replicating the unit cell of alpha-quartz to construct a crystalline model of SiO_2 and then raise the temperature to 10,000 K to melt the crystal and form liquid SiO_2. Next, by quenching the liquid to 300 K through intermediate temperatures, we obtain a solid block of a-SiO_2. In order to create a free surface for the a-SiO_2 substrate, we immobilize the atoms at the bottom of the block and remove the periodic boundary condition in the normal direction of the surface. Finally, the system is relaxed consecutively at 2000, 1000, and 300 K (10 ps at each temperature). This procedure generates an a-SiO_2 substrate with a macroscopically smooth surface. We note that more realistic surface structures of the a-SiO_2 substrate could be generated for MD simulations [54], including the surface roughness, but this is left for future studies.

3. Results and discussion

The traction–separation relations (σ–d) obtained from MD simulations are shown in Fig. 4(a)–(c) for three different water layer thicknesses. In each case, as the graphene is separated from the substrate, the water layer evolves from a continuous film to capillary bridges of different types, depending on the initial thickness of the water layer. The average traction first increases with increasing separation and then decreases. Eventually, the capillary bridge breaks up and the traction drops to zero. The area underneath the traction–separation curve gives the work of separation (per unit area), which may be different from the work of adhesion for the case of 'wet' adhesion due to possible hysteresis [55]. The work of separation is found to be 62.7, 70.7, and 66.9 mJ/m^2, respectively, for the three cases in Fig. 4. These values are close to the theoretical value (60.0 mJ/m^2) dictated by the interaction potential between graphene and water. While the interaction potential itself is short-ranged (less than 1 nm with an equilibrium separation at 0.274 nm [48]), the morphological evolution of water in the MD simulations results in interactions over a relatively long range (up to 3 nm). Meanwhile, the maximum traction is relatively low (about 90 MPa). Notably, the work of separation is

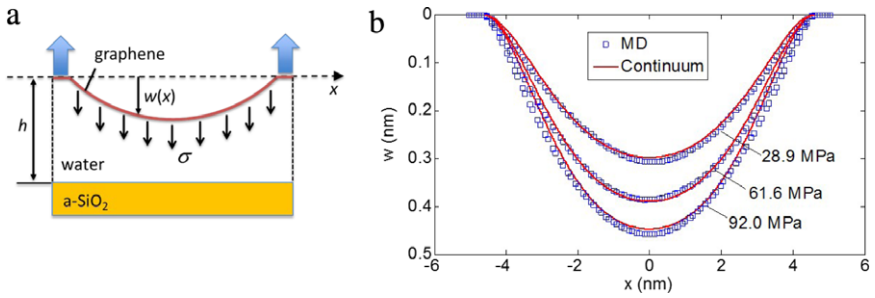

Fig. 5. (a) Illustration of a continuum model for a graphene sheet on a continuous water film, subjected to a uniform traction σ; (b) Deflections of graphene under three tractions, comparing the continuum analysis with MD simulations.

considerably smaller than the adhesion energy between graphene and dry SiO_2 (i.e. no water) by van der Waals interactions; the latter has been reported in the range of 0.1–0.45 J/m^2 [9–12]. This may be understood as a result of the hydrophobicity of graphene in the present model, which has a weaker graphene–water interaction than the direct graphene–SiO_2 interaction. On the other hand, the range of van der Waals interactions is shorter (less than 1 nm) [9]. Therefore, the presence of a water layer could effectively increase the range of interactions between graphene and the substrate, but the range is still much shorter than that reported in [15] based on large-scale experiments. Other effects such as surface roughness may have to be considered in future studies in order to close the gap.

In all three cases of Fig. 4(a)–(c), the traction–separation relations and the associated morphological evolution of water can be divided into three stages: (I) increasing traction with continuous water film (A–B), (II) decreasing traction with interfacial cavitation (B–D), and (III) decreasing traction with capillary bridging (D–G), as illustrated schematically in Fig. 4(d). While the traction–separation relations are similar in the three cases, the morphological evolution of water (especially cavitation and bridging) depends on the initial thickness of the water layer, as observed in the MD simulations with three different thickness values (Fig. 4(a)–(c)). In the following we discuss the three stages in detail with associated continuum analyses.

3.1. Stage I: Continuous water film

In the first stage of separation, the water remains a continuous film and undergoes a tensile deformation. Meanwhile, the graphene sheet deforms coherently as illustrated in Fig. 5(a). The interaction between graphene and water pulls the water up and drags the graphene down, whereas the hydrophilic interaction between water and a-SiO_2 keeps the water film attached to the substrate. The behavior of this stage can be analyzed approximately by a simple continuum model.

The graphene monolayer can be modeled approximately as a continuum plate [34] subject to a uniform normal traction σ with two clamped edges (Fig. 5(a)). The total potential energy of graphene is:

$$\Pi = \frac{DL}{2}\int_{-L/2}^{L/2}\left(\frac{\partial^2 w}{\partial x^2}\right)^2 dx + \frac{E_{2D}L}{2\left(1-\upsilon^2\right)} \times \int_{-L/2}^{L/2}\left[\frac{\partial u}{\partial x} + \frac{1}{2}\left(\frac{\partial w}{\partial x}\right)^2\right]^2 dx - \sigma L\int_{-L/2}^{L/2} w dx, \quad (3)$$

where L is the length of the square graphene sheet, E_{2D}, υ and D are in-plane Young's modulus, Poisson's ratio and bending modulus of graphene, w is the out-of-plane deflection and u is the in-plane displacement. The equilibrium deformation of graphene can be determined by minimizing the potential energy, leading to a set of nonlinear differential equations for $w(x)$ and $u(x)$. An approximate solution to the nonlinear problem takes the form [56]:

$$w(x) = \left(a_1 + a_2 x^2\right)\left(\frac{L^2}{4} - x^2\right)^2$$
$$u(x) = x\left(b_1 + b_2 x^2\right)\left(\frac{L^2}{4} - x^2\right), \quad (4)$$

where a_1, a_2, b_1 and b_2 are the parameters to be determined. Substituting (4) into (3), the total potential energy for graphene is obtained as a function of the four parameters, $\Pi(a_1, a_2, b_1, b_2)$. Minimizing the potential energy by setting $\frac{\partial \Pi}{\partial a_i} = 0$ and $\frac{\partial \Pi}{\partial b_i} = 0$ with $i = 1$ and 2, we obtain four algebraic equations that can be solved to determine the four parameters, with which we obtain the deflection profile for each given traction σ. To compare with MD simulations, the elastic properties of graphene predicted by the REBO potential [34] are used: $E_{2D} = 243$ N/m, $\upsilon = 0.397$, and $D = 1.4$ eV. Fig. 5(b) shows that the deflections of graphene predicted by the continuum analysis are in close agreement with the MD simulations.

Next, we consider deformation of the water film. With the deflection profile of graphene, the volume change of water can be calculated as:

$$\Delta V = L^2 d - L\int_{-L/2}^{L/2} w(x;\sigma)dx. \quad (5)$$

On the other hand, the volume change of the water film can be related to the traction by its constitutive behavior:

$$\Delta V = f(\sigma)V_0, \quad (6)$$

where $V_0 = L^2 h_0$ and $f(\sigma)$ is a nonlinear function for the hydrostatic stress–strain relation of the water film. Note that, by force balance, the hydrostatic tension in water equals the average traction acting on graphene; this is true under the condition that the interactions between graphene and a-SiO_2 are negligible. By Eq. (6), the function

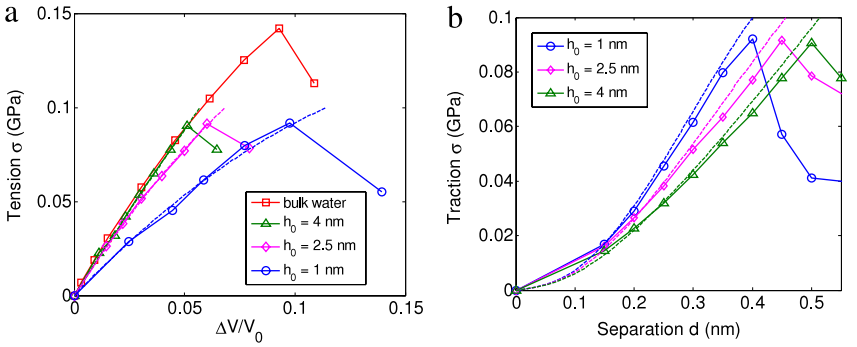

Fig. 6. (a) Volumetric stress–strain relations of water films with different initial thicknesses ($h_0 = 1$, 2.5 and 4 nm), in comparison with bulk water. The dashed lines show the fittings by Eq. (6) with a nonlinear function $f(\sigma)$ for each case. (b) Traction-separation curves for Stage I, comparing the continuum analysis (dashed lines) with the MD simulations (symbols).

$f(\sigma)$ can be obtained from MD simulations. It is found that $f(\sigma)$ depends on the initial thickness of the water film. As shown in Fig. 6(a), the stress–strain relation obtained from MD simulations is similar to the bulk water for a relatively thick water film ($h_0 = 4$ nm), but becomes more compliant for thinner water films. This may be attributed to the interfacial compliance between graphene and water, which becomes more important for thinner water films. By fitting the hydrostatic stress–strain curve in Fig. 6(a) with a nonlinear function $f(\sigma)$ for each case and combining Eq. (5)–(6), we obtain a traction–separation relation:

$$d(\sigma) = f(\sigma)h_0 + \frac{1}{L}\int_{-L/2}^{L/2} w(x;\sigma)dx. \tag{7}$$

As shown in Fig. 6(b), this relation compares closely with the MD simulations for the first stage up to the maximum traction (∼90 MPa). We note that the first term on the right-hand side of Eq. (7) depends on the initial thickness (h_0) of the water film. For a relatively thick water film ($h_0 \geq 4$ nm), $f(\sigma)$ is given by the constitutive behavior of bulk water, independent of h_0; hence the separation d increases linearly with h_0. For a thinner water film ($h_0 < 4$ nm), however, the dependence on the water thickness is more complicated since $f(\sigma)$ becomes thickness dependent. The second term on the right-hand side of Eq. (7) depends on the deformation of graphene, which also depends on the size of the graphene sheet (L). In general, we expect the separation to increase when the water thickness or the graphene sheet size increases in the first stage of separation.

The end of Stage I is marked by the maximum traction ($\sigma_m \sim 90$ MPa) in the traction–separation relation. Similar to the hydrostatic stress–strain behavior of bulk water in Fig. 2, the maximum traction is associated with cavitation of water. However, unlike the bulk water, cavitation of the water film occurs exclusively at the interface between water and graphene, due to relatively weak interactions across interface in the present model. As a result, the critical stress for cavitation is considerably lower for the water film than for bulk water (see Fig. 6(a)). Moreover, the maximum traction due to interfacial cavitation is independent of the water thickness (Fig. 6(b)), which defines an interfacial strength for the wet adhesion (i.e., pull-out stress). We note that the magnitude of the maximum traction depends on the interactions between water and graphene, or equivalently, the hydrophobicity of graphene. On the other hand, the corresponding separation at the maximum traction depends on the initial water thickness (Fig. 6(b)), which may be predicted by setting $\sigma = \sigma_m$ in Eq. (7). As discussed earlier, for relatively thick water films ($h_0 \geq 4$ nm), this separation increases linearly with h_0.

3.2. Stage II: cavitation growth

As observed in MD simulations, the growth of cavitation in the water film depends on the initial thickness h_0. For a relatively thick water film ($h_0 = 4$ nm), the cavity is nearly hemispherical (Fig. 7(a)–(c)), maintaining a 90° contact angle with graphene. The radius of the hemispherical cavity can be related to the surface tension of water (γ) and the average traction (σ) by force balance (Young–Laplace equation):

$$R = \frac{2\gamma}{\sigma}. \tag{8}$$

As the cavity radius increases, the traction σ decreases. The initial radius of the cavity is set by the maximum traction: $R_0 = 2\gamma/\sigma_m$, which defines a minimum thickness for the water film with a hemispherical cavity. In other words, if $h_0 < R_0$, the cavity cannot take the hemispherical shape, as discussed later.

The growth of a hemispherical cavity is limited by the size of the periodic box in the MD simulations, i.e., $R \leq L/2$, which sets a lower bound for the traction in Stage II:

$$\sigma_{II} = \frac{4\gamma}{L}. \tag{9}$$

When $R = L/2$, the neighboring cavities come into contact and coalesce, entering the next stage. The transition however often occurs when the neighboring cavities are sufficiently close but before contacting. Apparently, the size of the periodic box is arbitrarily set in the MD simulations, with no physical significance. A more realistic scenario may be that multiple cavities are nucleated over a large area and they grow independently until coalescence. The phenomenon is thus more complicated, beyond the scope of the present study. Nevertheless, we focus on

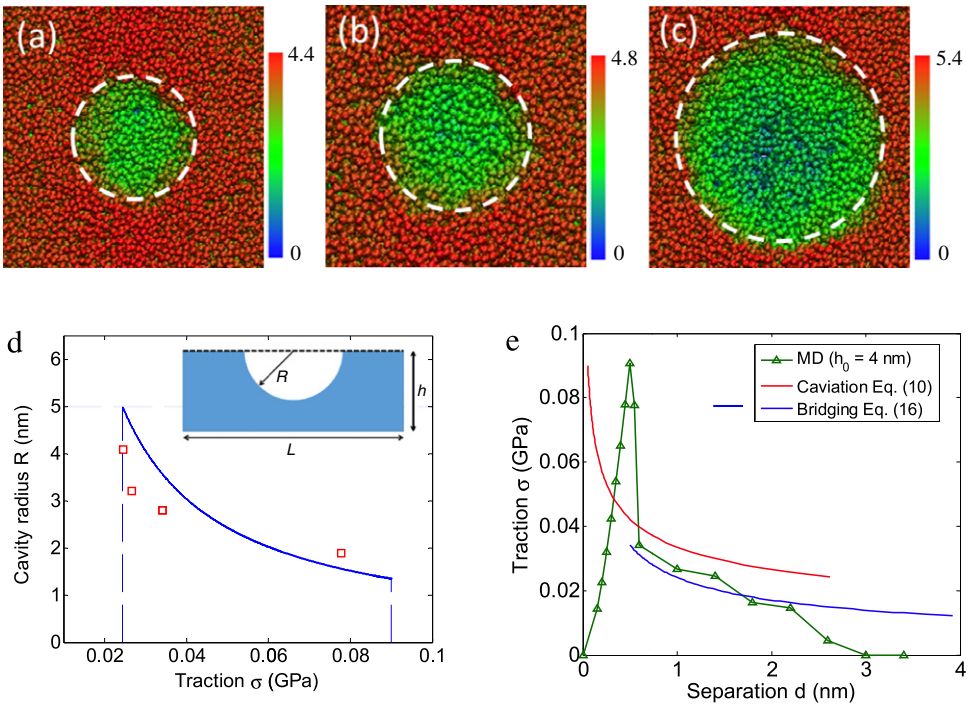

Fig. 7. Growth of a hemispherical cavity in a relatively thick water film ($h_0 = 4$ nm). (a)–(c) Snapshots of cavitation by MD simulations (top view, $\sigma = 77.7$, 34.2, and 24.6 MPa), showing water molecules colored by height contour (in nm). The nearly circular top of the cavity gives a measure of the radius, shown in (d) along with the prediction by Eq. (8). The inset in (d) shows schematic side view of a hemispherical cavity. (e) Traction-separation relation by MD in comparison with Eq. (10) for cavitation and Eq. (16) for capillary bridging. (For interpretation of the references to color in this figure legend, the reader is referred to the web version of this article.)

the traction–separation behavior due to cavitation growth assuming a fixed box size L.

Neglecting the volume change of water as well as deformation of graphene, the separation d can be related to the radius of the hemispherical cavity, which combines with Eq. (8) to yield a simple traction–separation relation for Stage II:

$$d(\sigma) = \frac{16\pi\gamma^3}{3L^2\sigma^3} \tag{10}$$

where $\sigma_m \geq \sigma \geq \sigma_{II}$. Thus, the maximum separation in Stage II is: $d(\sigma_{II}) = \pi L/12$. We note that the simple scaling, $d \sim \sigma^{-3}$, is a result of the constant volume assumption, without taking into account the thermodynamics of evaporation/condensation [57]. However, the effect of water volume change could be significant at high stresses. For example, at $\sigma = \sigma_m$, the volumetric strain of water is 5%–10% for the water films (Fig. 6(a)). Moreover, the deflection of the graphene monolayer could also be important in the present case. Without a detailed analysis of these effects, Eq. (10) serves as a rough estimate of the traction–separation relation in Stage II.

To compare with MD simulations, we take $\gamma = 0.0608$ N/m for the surface tension of water (discussed later). Fig. 7(d) compares the cavity radius from MD simulations with Eq. (8), and Fig. 7(e) compares the traction–separation relation (for $h_0 = 4$ nm) with Eq. (10). Overall the continuum analysis captures the qualitative trend for the cavitation growth and the traction–separation behavior in MD simulations (Stage II). The quantitative agreement could be improved by taking into account the volume change of water and the deflection of graphene in a more detailed continuum analysis.

By Eq. (8), taking $\sigma = \sigma_m \sim 90$ MPa and $\gamma = 0.0608$ N/m, the initiation radius of a hemispherical cavity is estimated to be $R_0 = 1.35$ nm. If the initial thickness of the water film is smaller than the initiation radius (i.e., $h_0 < R_0$), a non-spherical through-thickness cavity forms and grows, as observed in MD simulations for $h_0 = 1$ nm (see Fig. 8(a)–(c)). In this case, the cavitation growth can be analyzed approximately by assuming an axisymmetric cavity (see inset of Fig. 8(d)), governed by a couple of nonlinear differential equations:

$$\begin{cases} \dfrac{d\phi}{dz}\sin\varphi + \dfrac{\sin\varphi}{r} = \dfrac{\sigma_w}{\gamma} \\ \dfrac{dr}{dz}\sin\varphi = \cos\varphi, \end{cases} \tag{11}$$

where σ_w is the hydrostatic tension in water and the angle φ is a function of z with boundary conditions set by the contact angles: $\varphi = 0$ on the bottom surface ($z = 0$) and $\varphi = \pi/2$ on the top surface ($z = h$). The first equation in Eq. (11) is the Young–Laplace equation for the axisymmetric cavity, and the other equation is the geometric relation for the surface profile of the cavity, $r(z)$. In addition, assuming no volume change of water, we have

$$\int_0^h \pi r^2 dz = L^2 d, \tag{12}$$

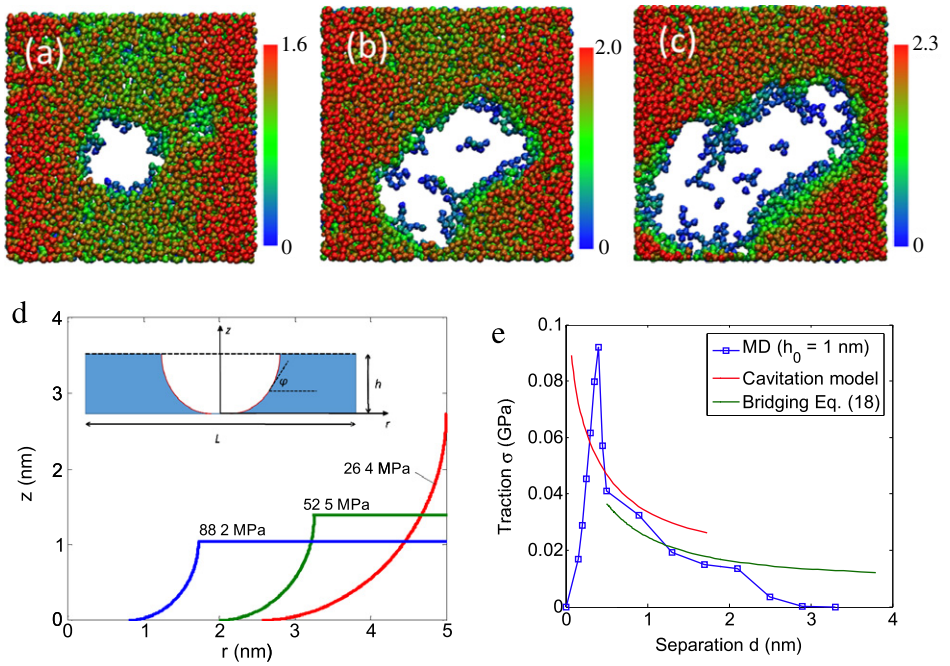

Fig. 8. Growth of a through-thickness cavity in a thin water film ($h_0 = 1$ nm). (a)–(c) Snapshots of cavitation by MD simulations (top view, $\sigma = 57.1, 32.5,$ and 19.2 MPa), showing water molecules colored by height contour (in nm) and exposure of the substrate surface. (d) Axisymmetric cavitation growth by a continuum analysis, showing the profiles corresponding to $\sigma = 88.2, 52.5,$ and 26.4 MPa. The inset shows the schematic side view of the cavitation model. (e) Traction-separation relation by MD in comparison with the axisymmetric cavitation model and Eq. (18) for the capillary bridging model. (For interpretation of the references to color in this figure legend, the reader is referred to the web version of this article.)

where $h = h_0 + d$. For a given water thickness ($h_0 < R_0$) and tension ($\sigma_w < \sigma_m$), the surface profile $r(z)$ and the corresponding separation d can be determined by an iterative procedure that numerically integrates Eq. (11) subject to the constraint in Eq. (12). The average traction acting on graphene is then, $\sigma = \sigma_w \left(1 - \pi r_0^2/L^2\right)$, where $r_0 = r(z = 0)$ is the radius of substrate exposure. Fig. 8(d) shows the surface profiles of the cavity at different traction levels for $h_0 = 1$ nm, and Fig. 8(e) shows the corresponding traction–separation relation. Starting at the maximum traction of 90 MPa, a through-thickness cavity is formed. As the cavity grows, the stress decreases and the separation increases until the radius of the cavity at the top reaches $L/2$ (5 nm) with a traction of 26.4 MPa. In comparison with MD simulations, the continuum analysis again qualitatively captures the traction–separation behavior in Stage II. However, the through-thickness cavity in the MD simulation does not take an axisymmetric shape in general, possibly due to the heterogeneous surface structures of the a-SiO_2 substrate.

The MD simulation for the case with a water film of thickness $h_0 = 2.5$ nm shows yet another scenario of cavitation growth: a nearly hemispherical cavity forms first, which grows and reaches the bottom of the water film, exposing the substrate surface (see Fig. 9). Again, assuming no volume change of the water, when the hemispherical cavity reaches the substrate surface, we have

$$L^2(R - h_0) = \frac{2}{3}\pi R^3. \tag{13}$$

For $R_0 \le R \le L/2$, Eq. (13) can be satisfied only if

$$R_0 \le h_0 \le \frac{2L}{3\sqrt{2\pi}}, \tag{14}$$

which defines a range of intermediate thickness for the water film. With $R_0 = 1.35$ nm and $L = 10$ nm, this range is between 1.35 and 2.66 nm. Indeed, the MD simulation with $h_0 = 2.5$ nm is in this range, whereas the case with $h_0 = 4$ nm (Fig. 7) is not and thus no substrate exposure. It may be expected that the corresponding traction–separation relation in this intermediate range lies in between of the previous two cases (i.e., hemispherical and through-thickness cavitation). For $h_0 = 2.5$ nm, a continuum analysis predicts a traction–separation relation very close to the case of hemispherical cavitation [48]. Similar to Fig. 7(e), the continuum analysis qualitatively captures the traction–separation behavior in Stage II.

3.3. Stage III: Capillary bridging

Cavitation growth in Stage II eventually leads to coalescence of neighboring cavities and the formation of capillary bridges. As shown in Fig. 10, by replicating the periodic box in the MD simulations, we see the morphological evolution of the capillary bridging in Stage III, from parallel ridges to circular islands. For the case of a thin water film ($h_0 = 1$ nm), the through-thickness cavities coalesce to form parallel ridges and islands with partially exposed substrate surface. For a relatively thick water film ($h_0 = 4$ nm), the ridges and islands form on top of a continuous water layer

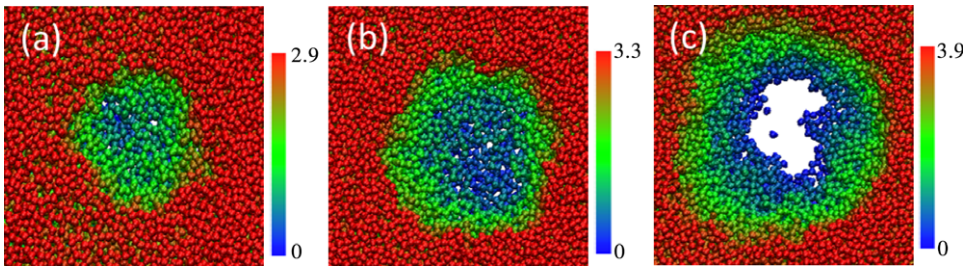

Fig. 9. Cavitation in a water film of intermediate thickness ($h_0 = 2.5$ nm) by MD simulations. (a)–(c) Plan-view snapshots for $\sigma = 78.5$, 26.7, and 21.8 MPa, showing water molecules colored by height contour (in nm) and exposure of the substrate surface in (c). (For interpretation of the references to color in this figure legend, the reader is referred to the web version of this article.)

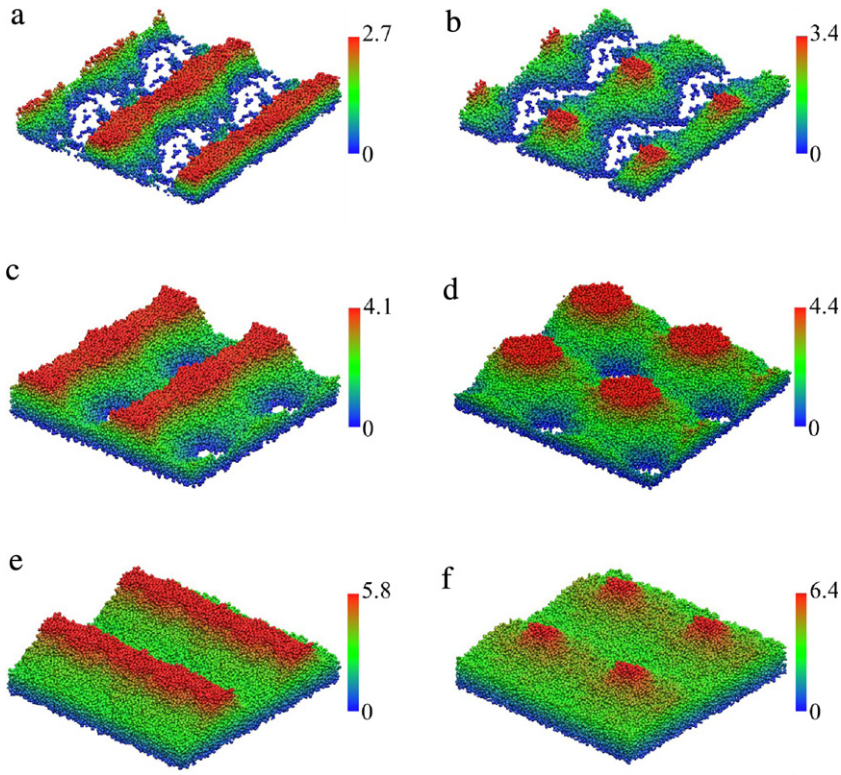

Fig. 10. Morphological evolution of capillary bridging between graphene and a-SiO_2 from MD simulations (2 by 2 periodic replication). (a)–(b) $h_0 = 1$ nm, $\sigma = 13.43$ and 3.54 MPa; (c)–(d) $h_0 = 2.5$ nm, $\sigma = 17.56$ and 9.56 MPa; (e)–(f) $h_0 = 4$ nm, $\sigma = 14.51$ and 4.59 MPa.

covering the substrate surface. For the case of an intermediate thickness ($h_0 = 2.5$ nm), the morphology is more complicated with an array of circular holes at the bottom of the water layer, along the ridges and in between of the circular islands. The morphological evolution of capillary bridging could influence the traction–separation behavior, although the MD results for the three cases in Fig. 4 are similar. It is possible to study the capillary bridging by numerical simulations based on continuum models [58,59]. In the present study, we consider two simple models, one for parallel water ridges and the other for circular islands.

Bridging with water ridges

The water bridging morphology in Fig. 10(e) can be described as parallel ridges on top of a blanket layer of water. Fig. 11 shows a cross-sectional view, where the side faces of the water ridge are approximately cylindrical with a radius R and the width of the ridge top is: $b = L - 2R$. The force balance requires that

$$R = \frac{\gamma}{\sigma}. \tag{15}$$

With $\sigma = 16.2$ MPa, $b = 2.5$ nm and $L = 10$ nm in Fig. 11, the surface tension of water can be determined by Eq. (15), giving $\gamma = 0.0608$ N/m. This value is in reasonable agreement with the typical value for surface tension of water (~0.07 N/m) and is used in all the continuum analyses of the present study for comparison with the MD simulations.

Again, by assuming no change of the water volume and neglecting the deflection of graphene, the separation is

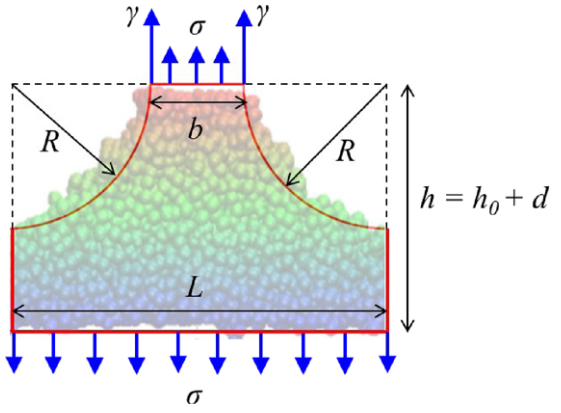

Fig. 11. Cross section of a water ridge bridging between graphene and a-SiO_2, comparing the continuum model (lines) with MD simulation (h_0 = 4 nm and σ = 16.2 MPa).

obtained as a function of the traction as

$$d(\sigma) = \frac{\pi R^2}{2L} = \frac{\pi \gamma^2}{2L\sigma^2}. \tag{16}$$

Fig. 11 compares the cross section of the water ridge from MD simulation with the continuum model (R = 3.75 nm and d = 2.21 nm). As the separation d increases, the traction σ decreases with a scaling relation, $d \sim \sigma^{-2}$; note that this scaling is different from that in Eq. (10) for cavitation growth in Stage II. Eventually, when $R = L/2$, the top of the ridge shrinks to a line ($b \to 0$), setting a lower limit for the traction, $\sigma_{III} = 2\gamma/L$, and the corresponding limit separation $d(\sigma_{III}) = \pi L/8$. The traction–separation relation by this continuum model is shown in Fig. 7(e) in comparison with MD simulation for the case with h_0 = 4 nm. Parallel ridges are observed in the MD simulation when the separation is around 2 nm. Since the traction in this stage is relatively low (<20 MPa), the effects of water volume change and graphene deflection are less significant so that the continuum model is fairly accurate. However, the parallel water ridges become unstable before the top width shrinks to zero, transitioning to water islands as shown in Fig. 10(f). This transition is similar to break-up of a liquid jet as a result of the Rayleigh instability [60,61], but with additional complexity due to the water–graphene interactions in the present case.

For the case of a thin water film (e.g., h_0 = 1 nm), the parallel water ridges become isolated with exposed substrate surface in between (Fig. 10(a)). For such isolated ridges, the average traction is related to the radius of the side face as

$$\sigma = \frac{\gamma(b + 2R)}{RL}, \tag{17}$$

where $b = Lh_0/R - (4 - \pi)R/2$ (assuming no volume change of water). The traction–separation relation is then

$$d(\sigma) = R - h_0 = \sqrt{\frac{2\gamma L h_0}{2\sigma L - \pi\gamma}} - h_0 \tag{18}$$

where the traction has a lower bound $\sigma_{III} = 2\gamma/L$ corresponding to $b = 0$. As shown in Fig. 8(e), Eq. (18) agrees with the MD results reasonably well in Stage III with 1–2 nm separation. Again, as the separation increases further, the parallel ridges become unstable and break up into islands (Fig. 10(b)).

Bridging with water islands

In the last stage of the separation process, the parallel water ridges break up to form water islands, similar to the Rayleigh instability [60,61]. While the water islands appear to be circular at the top interface, the morphology is more complicated in general (see Fig. 10(b), (d) and (f)). An approximate continuum analysis assuming an array of axisymmetric water islands on a continuous water film was performed [48]. However, under the constraint of the periodic box in MD simulations, no meaningful solution could be found for the cases considered in the present study (h_0 = 1–4 nm and L = 10 nm). A more sophisticated continuum analysis is necessary to capture the morphological evolution of the water bridging during this stage. Nevertheless, the results from the MD simulations (see Fig. 4) suggest that graphene is fully separated from the substrate soon after the formation of water islands.

4. Summary

MD simulations are conducted to study the traction–separation behaviors for wet adhesion between graphene and a-SiO_2. Three stages of the traction–separation relations are identified and they are analyzed approximately by simple continuum models. The work of separation (per unit area) is found to be close to the theoretical value (60.0 mJ/m^2) dictated by the interaction potential between graphene and water. The maximum traction is found to be set by the critical stress for cavitation at the water/graphene interface (around 90 MPa in the present study). With morphological evolution of water from cavitation to capillary bridging, the range of interaction extends to about 3 nm before complete separation of graphene. Compared to van der Waals interactions for dry adhesion between graphene and a-SiO_2, the work of separation for wet adhesion is considerably smaller, the maximum traction is lower, but the range of interaction is longer. It is noted that the properties of wet adhesion depend sensitively on the graphene-water interactions, which may vary considerably between hydrophobic and hydrophilic interactions.

Acknowledgments

The authors gratefully acknowledge financial support of this work by the National Science Foundation through Grant No. CMMI-1130261. The authors acknowledge the Texas Advanced Computing Center (TACC) at the University of Texas at Austin for providing HPC resources that have contributed to the research results reported within this paper.

References

[1] X.S. Li, Y.W. Zhu, W.W. Cai, M. Borysiak, B.Y. Han, D. Chen, R.D. Piner, L. Colombo, R.S. Ruoff, Transfer of large-area graphene films for high-performance transparent conductive electrodes, Nano Lett. 9 (2009) 4359–4363.

[2] S. Bae, H. Kim, Y. Lee, X. Xu, J. Park, Y. Zheng, J. Balakrishnan, T. Lei, H.R. Kim, Y. Song, Y. Kim, K. Kim, B. Ozyilmaz, J. Ahn, B.H. Hong, S. Lijima, Roll-to-roll production of 30-inch graphene films for transparent electrodes, Nature Nanotechnol. 5 (2010) 574–578.
[3] Y.M. Lin, C. Dimitrakopoulos, K.A. Jenkins, D.B. Farmer, H.Y. Chiu, A. Grill, P. Avouris, 100 GHz transistors from wafer-scale epitaxial graphene, Science 327 (2010) 662.
[4] S.R. Na, J.W. Suk, L. Tao, D. Akinwande, R.S. Ruoff, R. Huang, K.M. Liechti, Selective mechanical transfer of graphene from seed copper foil using rate effects, ACS Nano 9 (2015) 1325–1335.
[5] R. Huang, Graphene: Show of adhesive strength, Nature Nanotechnol. 6 (2011) 537–538.
[6] Z. Lu, M.L. Dunn, van der Waals adhesion of graphene membrane, J. Appl. Phys. 107 (2010) 044301.
[7] T. Li, Z. Zhang, Substrate-regulated morphology of graphene, J. Phys. D: Appl. Phys. 43 (2010) 075303.
[8] Z.H. Aitken, R. Huang, Effects of mismatch strain and substrate surface corrugation on morphology of supported monolayer graphene, J. Appl. Phys. 107 (2010) 123531.
[9] W. Gao, P. Xiao, G. Henkelman, K.M. Liechti, R. Huang, Interfacial adhesion between graphene and silicon dioxide by density functional theory with van der Waals corrections, J. Phys. D: Appl. Phys. 47 (2014) 255301.
[10] Z. Zong, C.L. Chen, M.R. Dokmeci, K.T. Wan, Direct measurement of graphene adhesion on silicon surface by intercalation of nanoparticles, J. Appl. Phys. 107 (2010) 026104.
[11] S.P. Koenig, N.G. Boddeti, M.L. Dunn, J.S. Bunch, Ultrastrong adhesion of graphene membranes, Nature Nanotechnol. 6 (2011) 543–546.
[12] N.G. Boddeti, S.P. Koenig, R. Long, J.L. Xiao, J.S. Bunch, M.L. Dunn, Mechanics of adhered, pressurized graphene blisters, J. Appl. Mech. 80 (2013) 040909.
[13] T. Yoon, W.C. Shin, T.Y. Kim, J.H. Mun, T.S. Kim, B.J. Cho, Direct measurement of adhesion energy of monolayer graphene as-grown on copper and its application to renewable transfer process, Nano Lett. 12 (2012) 1448–1452.
[14] Z. Cao, P. Wang, W. Gao, L. Tao, J.W. Suk, R.S. Ruoff, et al., A blister test for interfacial adhesion of large-scale transferred graphene, Carbon 69 (2014) 390–400.
[15] S.R. Na, J.W. Suk, R.S. Ruoff, R. Huang, K.M. Liechti, Ultra long-range interactions between large area graphene and silicon, ACS Nano 8 (2014) 11234–11242.
[16] A.W. Adamson, A.P. Gast, Physical Chemistry of Surfaces, Interscience Publishers, New York, 1967.
[17] Y.W. Chen, H.P. Cheng, Structure and stability of thin water films on quartz surfaces, Appl. Phys. Lett. 97 (2010) 161909.
[18] J.J. Yang, E.G. Wang, Water adsorption on hydroxylated alpha-quartz (0001) surfaces: From monomer to flat bilayer, Phys. Rev. B 73 (2006) 035406.
[19] M.J. Lee, J.S. Choi, J.S. Kim, I.S. Byun, D.H. Lee, S. Ryu, C. Lee, B.H. Park, Characteristics and effects of diffused water between graphene and a SiO_2 substrate, Nano Res. 5 (2012) 710–717.
[20] S. Wang, Y. Zhang, N. Abidi, L. Cabrales, Wettability and surface free energy of graphene films, Langmuir 25 (2009) 11078–11081.
[21] Y.J. Shin, Y. Wang, H. Huang, G. Kalon, A.T.S. Wee, Z. Shen, C.S. Bhatia, H. Yang, Surface-energy engineering of graphene, Langmuir 26 (2010) 3798–3802.
[22] K.-S. Kim, Hee-Jung Lee, C. Lee, S.-K. Lee, H. Jang, J.-H. Ahn, J.-H. Kim, H.J. Lee, Chemical vapor deposition-grown graphene: The thinnest solid lubricant, ACS Nano 5 (2011) 5107–5114.
[23] R. Raj, S.C. Maroo, E.N. Wang, Wettability of graphene, Nano Lett. 13 (2013) 1509–1515.
[24] F. Taherian, V. Marcon, N.F.A. van der Vegt, F. Leroy, What is the contact angle of water on graphene, Langmuir 29 (2013) 1457–1465.
[25] Z. Li, Y. Wang, A. Kozbial, G. Shenoy, F. Zhou, R. McGinley, P. Ireland, B. Morganstein, A. Kunkel, S.P. Surwade, L. Li, H. Liu, Effect of airborne contaminants on the wettability of supported graphene and graphite, Nature Mater. 12 (2013) 925–931.
[26] A. Kozbial, Z. Li, C. Conaway, R. McGinley, S. Dhingra, V. Vahdat, F. Zhou, B. D'Urso, H. Liu, L. Li, Study on the surface energy of graphene by contact angle measurements, Langmuir 30 (2014) 8598–8606.
[27] J. Dong, Z. Yao, T. Yang, L. Jiang, C. Shen, Control of superhydrophilic and superhydrophobic graphene interface, Sci. Rep. 3 (2013) 1733.
[28] J. Rafiee, X. Mi, H. Gullapalli, A.V. Thomas, F. Yavari, Y. Shi, P.M. Ajayan, N.A. Koratkar, Wetting transparency of graphene, Nature Mater. 11 (2012) 217–222.
[29] C.-J. Shih, Q.H. Wang, S. Lin, K.-C. Park, Z. Jin, M.S. Strano, D. Blankschtein, Breakdown in the wetting transparency of graphene, Phys. Rev. Lett. 109 (2012) 176101.
[30] S. Plimpton, Fast parallel algorithms for short-range molecular dynamics, J. Comput. Phys. 117 (1995) 1–19.
[31] D.W. Brenner, O.A. Shenderova, J.A. Harrison, S.J. Stuart, B. Ni, S.B. Sinnott, A second-generation reactive empirical bond order (REBO) potential energy expression for hydrocarbons, J. Phys.: Condens. Matter 14 (2002) 783–802.
[32] M. Arroyo, T. Belytschko, Finite crystal elasticity of carbon nanotubes based on the exponential Cauchy–Born rule, Phys. Rev. B 69 (2004) 115415.
[33] Y. Huang, J. Wu, K.C. Hwang, Thickness of graphene and single-wall carbon nanotubes, Phys. Rev. B 74 (2006) 245413.
[34] Q. Lu, R. Huang, Nonlinear mechanics of single-atomic-layer graphene sheets, Int. J. Appl. Mech. 1 (2009) 443–467.
[35] Q. Lu, W. Gao, R. Huang, Atomistic simulation and continuum modeling of graphene nanoribbons under uniaxial tension, Modelling Simul. Mater. Sci. Eng. 19 (2011) 054006.
[36] W. Gao, R. Huang, Thermomechanics of monolayer graphene: Rippling, thermal expansion and elasticity, J. Mech. Phys. Solids 66 (2014) 42–58.
[37] J. Tersoff, Modeling solid-state chemistry—interatomic potentials for multicomponent systems, Phys. Rev. B 39 (1989) 5566.
[38] S. Munetoh, T. Motooka, K. Moriguchi, A. Shintani, Interatomic potential for Si–O systems using Tersoff parameterization, Comput. Mater. Sci. 39 (2007) 334–339.
[39] H.J.C. Berendsen, J.R. Grigera, T.P. Straatsma, The missing term in effective pair potentials, J. Phys. Chem. 91 (1987) 6269–6271.
[40] J.-P. Ryckaert, G. Ciccotti, H.J. Berendsen, Numerical integration of the Cartesian equations of motion of a system with constraints: molecular dynamics of n-alkanes, J. Comput. Phys. 23 (1977) 327–341.
[41] R.W. Hockney, J.W. Eastwood, Computer Simulation using Particles, CRC Press, 2010.
[42] C.T. Chen, R.A. Fine, F.J. Millero, The equation of state of pure water determined from sound speeds, J. Chem. Phys. 66 (1977) 2142–2144.
[43] Q. Zheng, D.J. Durben, G.H. Wolf, C.A. Angell, Liquids at large negative pressures: water at the homogeneous nucleation limit, Science 254 (1991) 829–832.
[44] E. Herbert, S. Balibar, F. Caupin, Cavitation pressure in water, Phys. Rev. E 74 (2006) 041603.
[45] F. Caupin, Liquid–vapor interface, cavitation, and the phase diagram of water, Phys. Rev. E 71 (2005) 051605.
[46] J. Ma, A. Michaelides, D. Alfe, L. Schimka, G. Kresse, E.G. Wang, Adsorption and diffusion of water on graphene from first principles, Phys. Rev. B 84 (2011) 033402.
[47] T. Werder, J.H. Walther, R.L. Jaffe, T. Halicioglu, P. Koumoutsakos, On the water-carbon interaction for use in molecular dynamics simulations of graphite and carbon nanotubes, J. Phys. Chem. B 107 (2003) 1345–1352.
[48] W. Gao, Thermomechanical and interfacial properties of monolayer graphene (Ph.D. dissertation), The University of Texas at Austin, 2014.
[49] E.R. Cruz-Chu, A. Aksimentiev, K. Schulten, Water–silica force field for simulating nanodevices, J. Phys. Chem. B 110 (2006) 21497–21508.
[50] P.E.M. Lopes, V. Murashov, M. Tazi, E. Demchuk, A.D. MacKerell, Development of an empirical force field for silica. Application to the quartz–water interface, J. Phys. Chem. B 110 (2006) 2782–2792.
[51] N.T. Cuong, M. Otani, S. Okada, Semiconducting electronic property of graphene adsorbed on (0001) surfaces of SiO_2, Phys. Rev. Lett. 106 (2011) 106801.
[52] X.F. Fan, W.T. Zheng, V. Chihaia, Z.X. Shen, J.L. Kuo, Interaction between graphene and the surface of SiO_2, J. Phys.: Condens. Matter 24 (2012) 305004.
[53] D.A. Litton, S.H. Garofalini, Modeling of hydrophilic wafer bonding by molecular dynamics simulations, J. Appl. Phys. 89 (2001) 6013–6023.
[54] E. Paek, G.S. Hwang, A computational analysis of graphene adhesion on amorphous silica, J. Appl. Phys. 113 (2013) 164901.
[55] S. Cheng, M.O. Robbins, Capillary adhesion at the nanometer scale, Phys. Rev. E 89 (2014) 062402.
[56] S. Timoshenko, S. Woinowsky, Theory of Plates and Shells, McGraw-Hill, New York, 1959.
[57] H.-J. Butt, M. Kappl, Normal capillary forces, Adv. Colloid Interface Sci. 146 (2009) 48–60.
[58] F.M. Orr, L.E. Scriven, A.P. Rivas, Pendular rings between solids: meniscus properties and capillary force, J. Fluid Mech. 67 (1975) 723–742.
[59] J. Qian, H. Gao, Scaling effects of wet adhesion in biological attachment systems, Acta Biomater. 2 (2006) 51–58.
[60] L. Rayleigh, On the instability of jets, Proc. Lond. Math. Soc. 10 (1878) 4–13.
[61] J. Eggers, Nonlinear dynamics and breakup of free surfaces flows, Rev. Modern Phys. 3 (1997) 865–929.